Relict landscapes and fluvial landforms: Catastrophic outflow following a major Late Messinian base-level fall

Ninkabou D.[1,2], Gargani J.[3], Gorini C.[1], Rubino J-L.[2], Urgeles R.[4], Pellen R.[5], Do Couto, D. [1], Lethiers, A.[1], Haq, B.[1, 6], and Moneron, J. [1*] (corresponding author: jimmy.moneron@sorbonne-universite.fr)

[1] *ISTeP, Sorbonne Université, CNRS, 75005 Paris, France*

[2] *TotalEnergies E&P, 92078 La Défense, France*

[3] *GEOPS, Univ. Paris-Saclay, CNRS, 91405 Orsay, France*

[4] *Institut de Ciències del Mar (CSIC), 08003 Barcelona, Spain*

[5] *LGO, Univ. de Bretagne Occidentale, CNRS, 29280 Plouzané, France*

[6] *Smithsonian Institution, Department of Paleobiology, Washington DC, USA*

ABSTRACT

During the Messinian Salinity Crisis (MSC), the entire Mediterranean basin experienced deep canyon incision along its margins as the result of sea-level variations and rapidly increasing salinity. Yet, the processes and water sources capable of generating such dramatic incision have never been quantitatively demonstrated. Using high-resolution 3-D seismic reflection data and paleo-stream network geomorphic analyses, we reveal that a section of the Messinian Ebro valley is characterized by two distinct phases of fluvial dynamics. The initial phase is associated with an exceptional discharge of 240.10^3 m^3/s, rapidly carving a 700-m-deep valley, and is followed by a period with more moderate discharge through the newly formed Messinian valley,

forming alluvial terraces. Here we argue that the previously endorheic Ebro Basin was reached by regressive erosion during the MSC lowstand, triggering a major outburst flood and development of a wide and deep drainage system, transitioning to a more confined, meandering system. This study also refines the timing of this extraordinary outflow event to the MSC itself, contradicting earlier models that placed the Ebro Basin opening earlier. To the best of our knowledge, the complete drainage of an endorheic basin induced by a Messinian drawdown regressive erosion has not previously been described from the stratigraphic archive on Earth.

INTRODUCTION

Abrupt transitions in fluvial dynamics, such as those leading to catastrophic flooding, are rare, yet they mark some of the most dramatic episodes of landscape evolution on Earth (Gupta et al., 2007) and Mars (Warner et al., 2010). Such changes that manifest as major outflow events significantly affect continental-scale drainage patterns and are usually caused by climatic or sea-level change (Baker & Milton, 1974), or multi-causal factors leading to significant erosion (Loget et al., 2005). During the Messinian Salinity Crisis (MSC, 5.97-5.33 Ma, Krijgsman et al., 1999), major regressive erosion was induced in the context of major base-level variations (Chumakov, 1973, Ryan, 1976, Clauzon, 1982, Aloisi et al., 2025). The crisis, known for massive salt accumulation (Haq et al., 2020), is associated with the formation of the Messinian Erosional Surface (MES, Fig. 1), a key surface detected in continental margins all around the Mediterranean Sea (Guennoc et al., 2000; Lofi et al., 2005, Moneron et al., 2024).

With advancements in 3D seismic imagery, the delineation of these Messinian drainage systems improved, allowing further investigation of this MES and related Messinian Canyons (Urgeles et al., 2011; Moneron and Gvirtzman, 2022, Moneron et al. 2025), and although Messinian canyons are widely analyzed across Mediterranean margins (Gargani & Rigollet, 2007, Moneron et al., 2025), the mechanisms and hydrological conditions driving such deep erosion remain largely underexplored. Here, we examine Messinian landforms derived from a depth map of the MES, using topographic analysis tools to decipher the evolution of the paleo-Ebro River, akin to what is done on modern-day drainage systems. Based on a high-resolution 3D seismic reflection survey covering 2700 km² of the Ebro Margin (see Data and Methods in the Supplementary Material[1]), we identified a ~700 m-deep Messinian valley, raising the question of how a comparatively small basin such as the paleo-Ebro (~100,000 km²; Fig. 1) could have driven such extraordinarily rapid erosion. In what follows, we document the morphology and chronological development of the Ebro Canyon, quantify its hydrogeological evolution, and assess its role in this MSC large-scale event. This exceptional setting contrasts with earlier models proposing an earlier (13–8.5 Ma) basin opening by fluvial capture and sediment overfilling, with only minor influence from the Messinian sea-level fall (García-Castellanos et al., 2003, Urgeles et al., 2011).

BACKGROUND

The Ebro Drainage Before and During the MSC

Whereas the current Ebro River drains the Ebro foreland basin (between the Pyrenees and Iberian ranges (Fig. 1), the main Ebro Basin was once endorheic (i.e., self-contained) during the Oligo-Miocene, and formed in response to tectonic shortening (Nichols, 2004). When drainage was restricted to the endorheic basin, alluvial-lacustrine sediment accumulated only in the foreland from the Late Eocene to the Late-Middle Miocene (Riba et al., 1983; Perez-Rivarés et al., 2002; Fig. 1). It is argued that the formerly endorheic basin became externally drained through fluvial capture and sediment overfilling, with the Messinian sea-level fall likely exerting only a secondary influence, and the drainage shift of the Ebro Basin toward the Mediterranean occurring between roughly 13.5 and 8.5 Ma (García-Castellanos et al., 2003; Urgeles et al., 2011).

Despite the progradation of coastal/deltaic deposits on the Ebro margin (Evans & Arche, 2002), no major Late Messinian fluvial incision is identified onshore. Consequently, the Messinian Ebro valley must have been relatively short in length, and regressive erosion was not extensive onshore, unlike other Messinian Mediterranean rivers (*e.g.,* Nile and Rhône rivers; Pellen et al., 2019).

On the Ebro margin in the western Mediterranean, the MES is manifested on seismic profiles by erosional truncations of the top of Miocene clinoforms (Urgeles et al., 2011; Fig. 1B). It is also characterized in this area by a broad incised valley attributed to the paleo-Ebro River system (Urgeles et al., 2011).

The area of interest (Fig. 1) is located on the proximal-most part of the Ebro fluvial incision, characterized by several knickpoints along the system (Pellen et al., 2019). In this area, the MES is represented by a proximal, high relief region (Region I in Fig. 2) and distal low-relief area (Pellen et al., 2019, region II & III, Fig. 2). Both regions, initially documented by Urgeles et al. (2011), are parallel to the present-day coastline.

RESULTS

The Messinian Ebro River

Mapping of the MES reveals the presence of vast channelized features, aggrading above the Messinian paleo-landscape (Fig. 2). In region I, a major NW-SE, 2km wide valley, with ~1300 m of relief is visible over a map of the MES, with two major valleys (N-S and E-W) serving as tributaries of the main valley (Fig. 2A-C). Downstream, the valley widens to 3.5km in region II and up to ~4km in region III (Fig. 2).

The first channel (dubbed "C0") which is also the widest (width from 500m upstream up to 3500m downstream), is characterized by a high amplitude seismic reflector, also clearly visible in map-view, within a flat-based valley (Fig. 2A-C) with infilled morphology, overbank deposits and associated splays (Fig 2A-C). Its thalweg is mainly straight (sinuosity: 1.1) over the studied area. Further downstream secondary channelized systems (C1 to C4) clearly crosscut and overprint C0. C1, the deepest and longest system (Fig. 2A), is fed downstream by converging tributaries (C2 to C4). Although C0 and C1 share a common upstream thalweg (Fig. 2A), C1 remains confined throughout its path toward the deep basin while C0 is wider starting about 10 km downstream from the channel head. C1 then narrows relative to C0, with widths reaching 500–650 m in its deepest section. Numerous meanders are observed (mean sinuosity: 1.4 to 1.7) along its path.

Discharge Estimates and Topographic Analyses

The map of the MES was analyzed (See Methods in the Supp Mat.[1]) to assess the features of the Messinian topography (Fig. 3A). The catchment of the channels C1 to C3 is estimated to be at least 1070 km^2 (Fig. 3A). The longitudinal stream profiles show that the main trunk (C1) has the gentlest profile compared to C2 and C3 (Fig. 3A, 3D). The stream profiles also show knickpoints on channels C2 and C3 (Fig. 3D).

To calculate River discharges, we used two approaches: one based on channel width (Fig. 3B, Fig. S3, Attal et al., 2008) and another applying Manning's equation (Fig. 3B-C, Fig. S2, Table S1). We calculated a discharge of C0 that reached ~2.4×10^5 m^3/s, indicating an extraordinary outflow regime (Figs. 3A, 3C). Fig. 3B reveals that in the downstream part of C0-C1, alluvial terraces are visible. Incising C0, where these terraces are found (Fig. 3B), the mean discharge estimated for C1 7.2 10^3 m^3/s, with a peak discharge downstream at $14.7 \cdot 10^3$ m^3/s (Fig. 3C, 3E). Discharge values estimated from both methods (Manning formula and the width of C1) yield similar results (Fig. 3) and show an increase in downstream discharge after C2-C4 merged with C1, as expected for fluvial systems. Both methods indicate lower discharge for C1 than for C0, suggesting an initial abrupt outflow from the Ebro endorheic basin, followed by more moderate flow (C1–C4) (Fig. 3B) (See Discussion).

Further analysis of the topography of the drainage system shows a value of the Hack's law h-constant of ~0.48 (Rigon et al., 1996; Hergarten et al., 2015). While the *h*-constant is usually 0.6-0.5 , deviation from this value may indicate a large drop of the base-level of these paleo-streams (Fig. 3D). Flint's law analyses yields a concavity index (θ) of 0.30° and channel steepness (k_s) of ~8.2 (Fig. 3E), values usually related to margins subject to uplift (Hergarten et al., 2015, Bahia et al., 2019).

DISCUSSION

Can Climatic Conditions Alone Explain the Formation of Major MSC Rivers?

While it has been argued that the opening of the Ebro Basin (1) started long before the MSC; and (2) was probably due facilitated by periods of wetter climatic conditions (Garcia-Castellanos et al., 2003; Urgeles et al., 2011), our results suggest a different story. Although major discharge in rivers can be historically explained by climatic changes (i.e., from arid to wet), this exceptional outflow (~2.4×10^5 m^3/s) is 20 times higher than that of the Ebro River historic floods of 1787 and 1907, which reached a peak discharge of 12.9×10^3 m3/s and $11.5 \cdot 10^3$ m^3/s Balasch et al., 2019), respectively. The estimated value is in the range of apparent paleo-discharges observed for outburst floods such as that in Lake Agassiz (*i.e.,* $100\text{-}600 \cdot 10^3$ m^3/s, Tinkler & Pengelly, 1995) but lower than flooding discharge estimated during the MSC on the Gibraltar sill (10^8 m^3 s^{-1}, Garcia-Castellanos et al., 2009) and on the Sicilian sill (47.4 10^6 m^3s^{-1}, Spatola et al., 2020). The estimated apparent paleo-discharge of C1 ($7.2 \cdot 10^3$ m^3/s) is in the same range or lower than the maximum historical flood of the Ebro River in 1787 and 1907 ($10.5.10^3$ $-12.9 \cdot 10^3$ m^3/s; Ruiz-Bellet et al., 2017, Balasch et al., 2019).

Despite generally arid conditions in the western Mediterranean, the Messinian Ebro margin experienced comparatively wetter climates and higher mean precipitation (Fauquette et al., 2006), consistent with the observed channel morphology and inferred discharges following the major C0 outflow. Moreover, the lack of chaotic reflections or amphitheater-shaped heads in the 3D seismic data, together with continuous reflectors and well-preserved meanders, points to a dominantly fluvial origin governed by discharge dynamics rather than slope failure or sapping due to extreme climatic conditions.

Taken together, these observations indicate that only a catastrophic lake-outburst flood can account for such extreme flow within a basin of this size. We therefore infer that the Ebro paleo-lake was fully drained during the Messinian sea-level fall, its outburst explaining the scale and morphology of channel C0.

Driving Mechanisms and Chronology of Events

This study provides the first documentation of a basin-scale response to the MSC: the complete drainage of an endorheic lake system induced by base-level fall (Fig. 4A-B). The resulting outflow represents a previously unrecognized mechanism linking Mediterranean drawdown to continental drainage reorganization. Notably we provide the first evidence of Messinian alluvial terraces, documenting post-outburst fluvial re-incision, probably contemporaneous with flexural uplift (see Figure S9).

The pronounced ~1300 m relief of the MES (Fig. 4A-B) was generated between the onset of Mediterranean drawdown (~5.60 Ma) and the ensuing transgressive stage (~5.36 Ma; Pellen et al., 2019), implying erosion rates of 5.4–9.3 mm/yr, values comparable to the most rapidly incising modern landscapes (Hergarten & Kenkmann, 2019). The stacked C0–C1 terraces record at least ~150 m (Figs. 2-3) of relative vertical motion during the MSC, indicating renewed incision following the initial lake outburst. This vertical offset likely reflects a second phase of deformation linked to isostatic rebound, superimposed on the broader flexural response to Mediterranean drawdown. (see Fig. S9 for additional details regarding isostatic rebound calculations).

Here, our observations collectively indicate that canyon incision along the Ebro margin reached its peak during the lowstand phase of the MSC, when rapid regressive erosion triggered the opening of the Ebro endorheic basin and a short-lived but catastrophic lake outburst flood (Fig. 4C, t_1–t_2). This event excavated the broad, high-discharge channel C0 and initiated deep canyon formation. The subsequent decrease in discharge during continued lowstand conditions and flexural isostatic rebound allowed for renewed incision by narrower, meandering channels (C1–C4; Fig. 4, t_3) and formation of alluvial terraces, consistent with a transition from catastrophic outflow to sustained fluvial reorganization as base level and hydrological conditions stabilized. The return to normal marine conditions led to progressive burial of the Messinian landscape under Pliocene–Quaternary sediments, preserving its relict fluvial morphology Fig. 4C, t_4).

From a broader perspective, this interpretation also contrasts with earlier models proposing that the Ebro Basin opened well before the Messinian (13-8.5 Ma), through fluvial capture and progressive sediment overfilling, with the Messinian sea-level fall playing only a minor role (García-Castellanos et al., 2003). Our results instead point to a later, MSC-linked drainage event, in which the rapid base-level fall directly triggered basin breaching and catastrophic lake outflow.

CONCLUSION

This work provides the first integrated evidence that the MSC triggered the complete drainage of an endorheic basin through base-level fall. The Ebro margin underwent two successive fluvial phases: an initial lake outburst flood formed during Mediterranean drawdown, followed by a lower-energy, meandering system incised under continued regressive erosion and isostatic rebound. These results refine the timing of the Ebro Basin opening, demonstrating that external drainage developed synchronously with the late Messinian lowstand at odds with what was previously proposed. The fluvial landforms were then preserved under a thick sedimentary unit, offering a rare record of transient canyon formation and rapid landscape adjustment to extreme base-level change.

ACKNOWLEDGMENTS

This work was done in the scope of the *Seismic Geomorphology* research project of TotalEnergies SE, which we thank for providing access to seismic data and a SISMAGE license. We thank former GEOLOGY Science Editor William Clyde for his valuable feedback and suggestions. The constructive feedback and insightful suggestions from Mike Blum, Andrew Madof, and an anonymous reviewer significantly improved the quality of this manuscript.

REFERENCES CITED

Aloisi, G., Moneron, J., Guibourdenche, L., Camerlenghi, A., Gavrieli, I., Bardoux, G., Agrinier, P., Ebner, R., and Gvirtzman, Z., 2024, Chlorine isotopes constrain a major drawdown of the Mediterranean Sea during the Mes sinian salinity crisis: Nature Communications, v. 15, 9671, https://doi .org /10 .1038 /s41467-024-53781-6.

Attal, M., Tucker, G. E., Whittaker, A. C., Cowie, P. A., and Roberts, G. P., 2008, Modeling fluvial incision and transient landscape evolution: Influence of dynamic channel adjustment, J. Geophys. Res., 113, F03013, doi:10.1029/2007JF000893.

Bahia, R., Jones, M., Covey-crump, S.J., & Mitchell, N.C., 2019, The application of Hack's law and Flint's law to Mars and its implications for the Noachian climate (LPI contribution No. 2132).

Baker, V.R., Milton, D.J., 1974, Erosion by catastrophic floods on Mars and Earth. Icarus 23, 27–41.

Balasch J.C., Pino D., Ruiz-Bellet J.L., Tuset J., Barriendos M., Castelltort X., Peña J.C., (2019). The extreme floods in the Ebro River basin since 1600 CE, Science of The Total Environment, v.646, 645-660.

Chumakov, I. S., (1973), Pliocene and Pleistocene deposits of the Nile valley in Nubia and upper Egypt, Initial Rep. Deep Sea Drill. Proj., 13, 1242- 1243.

Clauzon, G., 1982, Le canyon messinien du Rhône: Une preuve decisive du desiccated deep-basin model (Hsü , Cita et Ryan, 1973), Bull. Soc. Géol. Fr., 24, 597–610

Evans, G., Arche, A., 2002, The flux of siliciclastic sediment from the Iberian Peninsula, with particular reference to the Ebro. In: Jones SJ, Frostick LE (eds) Sediment flux to basins: causes, controls and consequences. Geol Soc Spec Publ, London, pp 199–208

Fauquette, S., Suc J-P., Bertini A., et al., 2006, How much did climate force the Messinian salinity crisis? Quantified climatic conditions from pollen records in the Mediterranean region, Palaeogeogr. Palaeoclimatol. Palaeoecol., 238, 281– 301.

Garcia-Castellanos, D., J. Vergés, J.M. Gaspar-Escribano and S. Cloetingh, 2003, Interplay between tectonics, climate and fluvial transport during the Cenozoic evolution of the Ebro Basin (NE Iberia).J. Geophys. Res. 108 (B7), 2347. doi:10.1029/2002JB002073.

García-Castellanos, D., Estrada, F., Jimenez-Munt, I., Gorini, C., Fernandez, M., Verges, J., & De Vicente, R. (2009). Catastrophic flood of the Mediterranean after the Messinian salinity crisis. *Nature*, *462*(7274), 778-781.

Gargani, J., Rigollet, C., Scarselli, S., 2010, Isostatic response and geomorphological evolution of the Nile valley during the Messinian salinity crisis. Bull. Soc. Geol. Fr., v.181, n.1, p.19-26.

Guennoc, P., Gorini, C., Mauffret, A., 2000. Geological history of the Gulf of Lions: Oligo-Aquitanian rift and Messinian surface maps. Histoire geologique du golfe du Lion et cartographie du rift oligo-aquitanien et de la surface messinienne Geol. Fr. 3, 67e97.

Gupta, S., Collier, JS., Palmer-Felgate, A., Potter. G., et al., 2007, Catastrophic flooding origin of shelf valley systems in the English Channel, Nature, Vol: 448, Pages: 342-U5

Haq, B., Gorini, C., Baur, J., Moneron, J., and Rubino, J. L., 2020, Deep Mediterranean's Messinian evaporite giant: How much salt?. Global and Planetary Change, 184, 103052. doi: https://doi.org/10.1016/j.gloplacha.2019.103052

Hergarten, S., & Robl, Jörg & Stüwe, Kurt , 2015, Tectonic geomorphology at small catchment sizes -extensions of the stream-power approach and the -method. Earth Surface Dynamics Discussions. 3. 689-714. doi.org/10.5194/esurfd-3-689-2015.

Hergarten, S., & Kenkmann, T., 2019, Long-term erosion rates as a function of climate derived from the impact crater inventory. Earth Surface Dynamics, 7(2). doi: 10.5194/esurf-7-459-2019

Hsü, K. J., Cita, M. B., and Ryan, W. B. F., (1973), The origin of the Mediterranean evaporites, in Kaneps, A. G., ed., Initial reports of the deep sea drilling project, Volume 13: Washington, D. C., U. S. Government Printing Office, p. 1203-1231.

Krijgsman, W., Hilgen, F. J., Raffi, I., Sierro, F. J. & Wilson, D. S., 1999, Chronology, causes and progression of the Messinian salinity crisis. Nature 400, 652–655.

Lofi, J., Gorini, C., Berné, S., Clauzon, G., Dos Reis, A. T., Ryan, W. B., & Steckler, M. S. (2005). Erosional processes and paleo-environmental changes in the Western Gulf of Lions (SW France) during the Messinian Salinity Crisis. *Marine Geology*, *217*(1-2), 1-30.

Loget, N., Driessche, J. V. D., & Davy, P. (2005). How did the Messinian salinity crisis end?. *Terra Nova*, *17*(5), 414-419.

Moneron, J., and Gvirtzman, Z., 2022, Late Messinian submarine channel systems in the Levant Basin: Challenging the desiccation scenario: Geology, v. 50, p. 1366–1371, https://doi .org /10 .1130 /G50583 .1.

Moneron, J., Gvirtzman, Z., Karcz, Z., and Sagy, Y., 2024, Discovery of the Messinian Eratosthenes Canyon in the deep Levant Basin: Global and Planetary Change, v. 232, https://doi .org /10 .1016 /j .gloplacha .2023 .104318.

Moneron, J., Gvirtzman, Z., Karcz, Z., Shitrit, O., Sagy, Y., and Aharonov, E., 2025, Exploring the relationship between sedimentary transport systems and basin dy namics: A case study from the Levant Basin (Eastern Mediterranean Sea) before, during, and after the Mes sinian: Geological Society of America Bulletin, v. 137, p. 1423–136, https://doi .org /10 .1130 /B37589 .1.

Nichols, G., 2004, Sedimentation and base level in an endorheic basin : the early Miocene of the Ebro Basin , Spain.

Pellen, R., Aslanian, D., Rabineau, M., Suc, J. P., Gorini, C., Leroux, E., ... and Rubino, J. L. , 2019, The Messinian Ebro River incision. Global and Planetary Change, 181, 102988. doi: https://doi.org/10.1016/j.gloplacha.2019.102988

Pérez-Rivarés, F.J., Garcés, M., Arenas, C., and Pardo, G., 2004, Magnetostratigraphy of the Miocene continental deposits of the Montes de Castejón (central Ebro basin, Spain): Geochronological and paleoenvironmental implications: Geologica Acta, v. 2, p. 221–234.

Riba, O., Reguant, S., and Villena, J., 1983, Ensayo de síntesis estratigráfica y evolutiva de la cuenca terciaria del Ebro, in Comba, J., ed., Libro Jubilar J. M. Ríos, Geología de España, Volume 2: Madrid (Spain), Instituto Geológico y Minero de España, p. 131-159.

Rigon, R., I. Rodriguez-Iturbe, A. Maritan, A. Giacometti, D. G. Tarboton, and A. Rinaldo (1996), On Hack's Law, Water Resour. Res., 32(11), 3367–3374, doi:10.1029/96WR02397.

Ruiz-Bellet, J.L., Castelltort, X., Balasch, J.C., and Tuset, J., 2017, Uncertainty of the peak flow reconstruction of the 1907 flood in the Ebro River in Xerta (NE Iberian Peninsula). Journal of Hydrology, 545, 339-354.

Ryan W.B.F., 1976. Quantitative evaluation of the depth of the western Mediterranean before, during and after the Late Miocene salinity crisis. Sedimentology, v.23, n.6, p. 791-813.

Spatola D., del Moral-Erencia J.D., Micallef A., Camerlenghi A., Garcia-Castellanos D., Gupta S., Bohorquez P., Gutscher M.-A., Bertoni C., 2020. A single-stage megaflood at the termination of the Messinian salinity crisis: Geophysical and modelling evidence from the eastern Mediterranean Basin. Marine Geology, v.430, 106337.

Tinkler, K.J., Pengelly ,J.W.J., 1995. Great Lakes response to catastrophic inflows from Lake Agassiz: some simulations of a hydraulic geometry for chained lake systems. Journal of Paleolimnology, Volume 13, Issue 3, pp 251–266

Urgeles, R., Camerlenghi, A., García-Castellanos, D., De Mol, B., Garcés, M., Vergés, J., Haslam I., Hardman, M., 2010. New constraints on the Messinian sealevel drawdown from 3D seismic data of the Ebro Margin, Iberian Peninsula, and implications for the evolution of the Ebro Basin. Basin Res. , doi: https:/doi/org/10.1111/j.1365-2117.2010.00477.x

Warner, N, Gupta, S, Muller, J-P, Kim, J-R, Lin, S-Y , 2009, A refined chronology of catastrophic outflow events in Ares Vallis, Mars, Earth and Planetary Science Letters, Vol: 288, Pages: 58-69

FIGURE CAPTIONS

Fig. 1. A. Map showing study area on the Ebro margin, western Mediterranean Sea, offshore NE Spain. Black polygon outlines the extent of the 3D seismic dataset used in this study. Messinian river incision (in dark red, from Pellen et al., 2019) affected all Mediterranean margins, including the Valencia Trough and Gulf of lions. Inset of A is from Haq et al., 2020. **B**. Typical cross section showing the MES and prograding Plio-Quaternary sediments. Inset of B is modified after Lofi et al., 2005. More regional seismic cross sections are provided in the Supp. Mat.[1] (Fig. S4). AOI-Area of interest, L-PB--Liguro-Provençal Basin ALB—Algero-Balearic Basin.

Fig. 2. A-B MES depth map and morphological features in the Ebro valley during the MSC: C0 represents the outflow channel and C1-C4, the meandering channel observed with 3D seismic data. Seismic sections indicated on the map are shown in Fig. S5, and more 3D visualizations are shown in Fig. S6-8. **C**. 3D view of the main channel C0 being crosscut by the C1 meandering channel. **D-D', E-E'**. Seismic sections illustrating the vertical and lateral arrangement of channels C0-C4. See Fig. S10 for uninterpreted version of A. Grid resolution is 12.5m.

Fig. 3. A. Drainage map extracted from the Messinian Erosional Surface (MES) showing the main channel network (C1–C3) and its ~1070 km^2 catchment. **B**. Cross-section showing channel C1 incising the earlier high-discharge channel C0. **C**. Quantitative approach for discharge estimation using Manning's equation. The area where calculations were made for C0 is shown in Fig. 3A. **D**. Longitudinal stream profiles highlighting knickpoints in C2–C3. **E.** Discharge estimates for C1 derived from Manning's law and width–area scaling. **F**. Stream length–area and slope–area relationships fitted to Hack's and Flint's laws.

Fig. 4. A–B 3D geomorphic framework showing the Messinian Erosional Surface (MES) paleo-relief, and channel organization (C0–C4). **C** Four-stage model illustrating the transition from sea-level drawdown and regressive erosion (t_1), to catastrophic lake outburst, canyon formation and accumulation of C0 deposits (t_2), renewed incision by meandering channels C1–C4 under lowstand conditions (t_3), and final burial during Pliocene–Quaternary (P-Q) sedimentation (t_4).

FIGURES

Figure 1

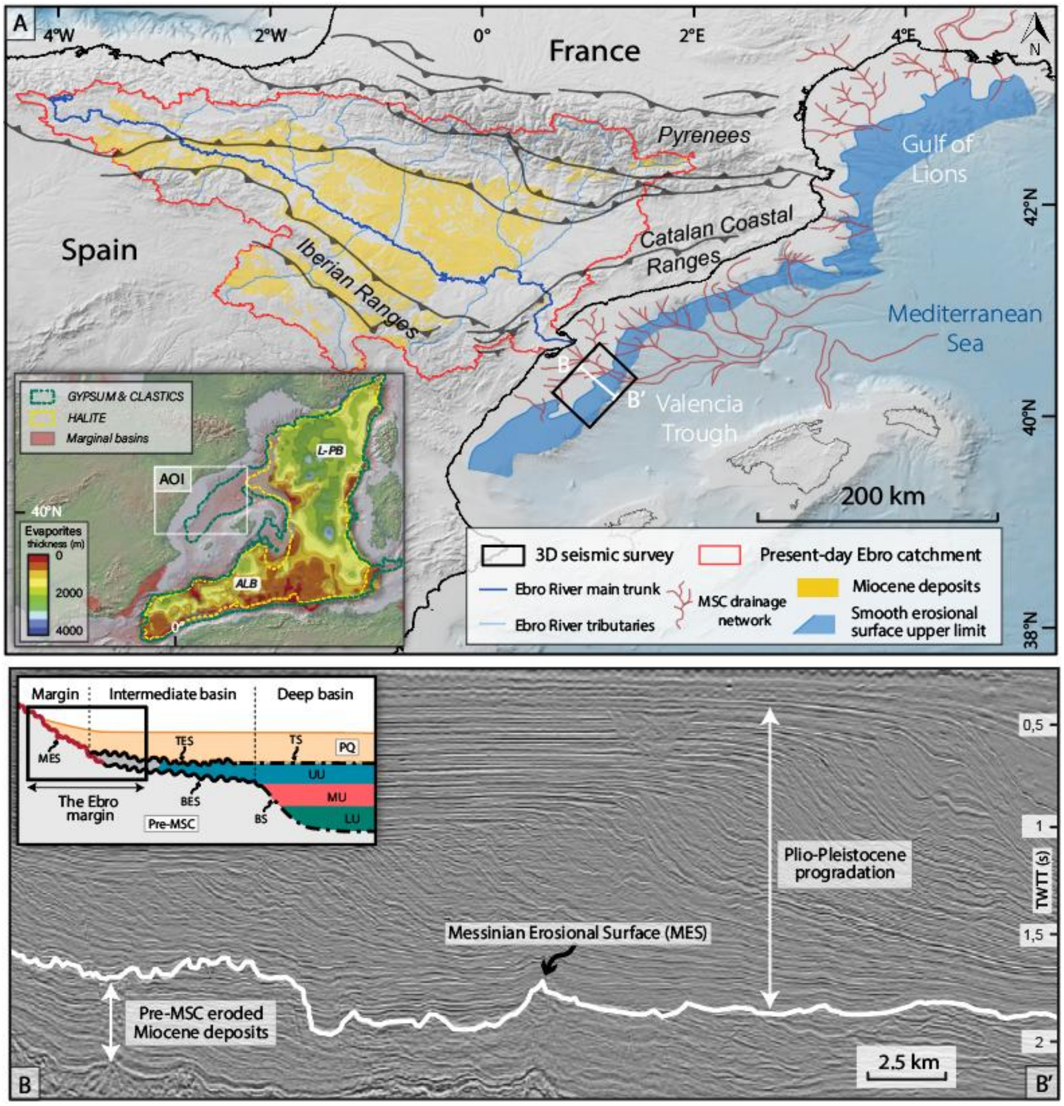

Figure 2

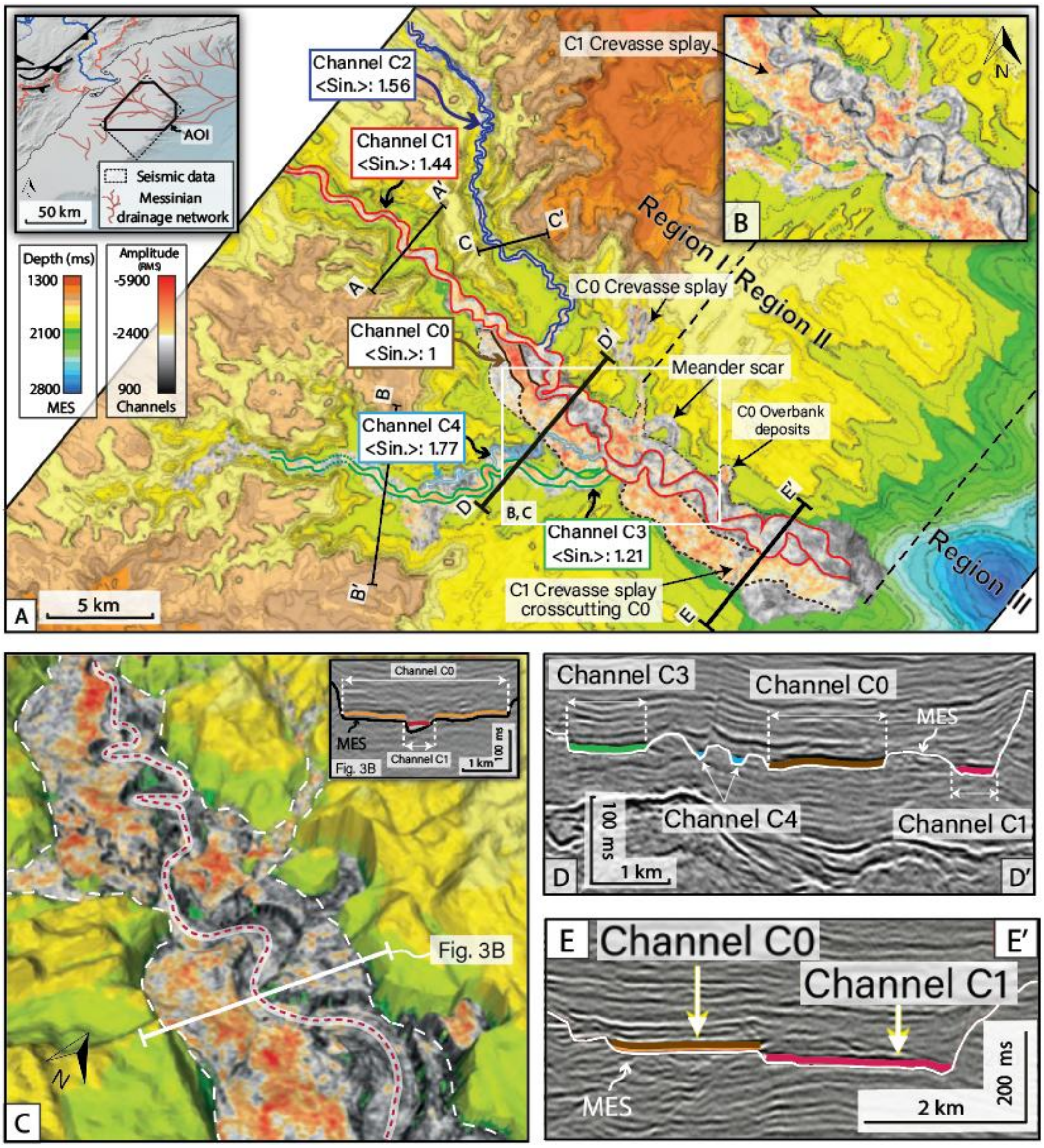

Channel C2
<Sin.>: 1.56
Channel C1
<Sin.>: 1.44
Channel C0
<Sin.>: 1
Channel C4
<Sin.>: 1.77
Channel C3
<Sin.>: 1.21
C1 Crevasse splay crosscutting C0
C0 Crevasse splay
Meander scar
C0 Overbank deposits
C1 Crevasse splay
Region I
Region II
Region III
AOI
Seismic data
Messinian drainage network
50 km
5 km
Depth (ms)
1300
2100
2800
MES
Amplitude (RMS)
-5900
-2400
900
Channels
B, C
A
B
C
D
E
N
Fig. 3B
Channel C0
Channel C1
MES
1 km
100 ms
Channel C3
Channel C0
MES
Channel C4
Channel C1
100 ms
1 km
D
D′
E
E′
Channel C0
Channel C1
MES
2 km
200 ms

Figure 3

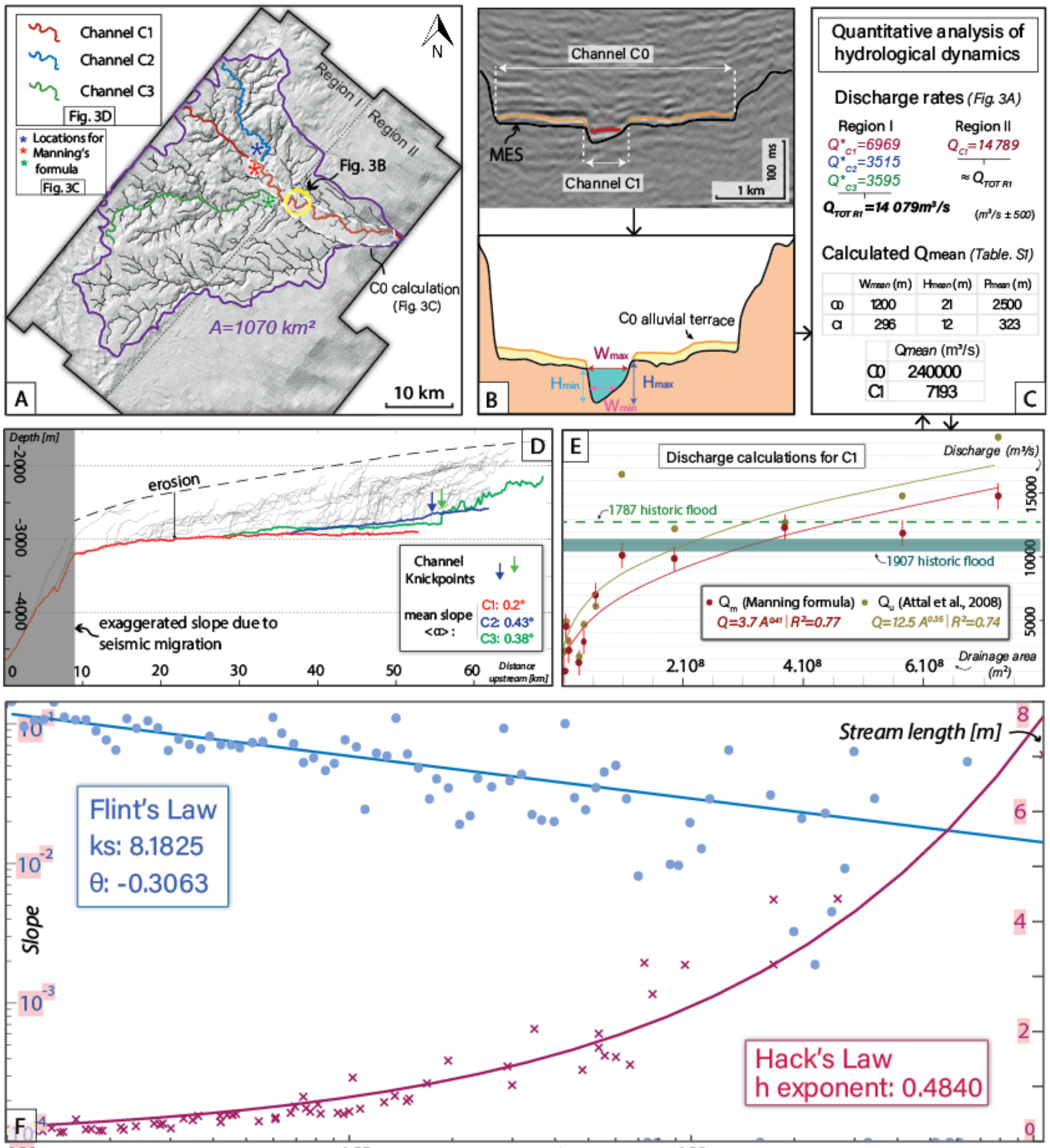

Channel C1
Channel C2
Channel C3
Fig. 3D
Locations for Manning's formula
Fig. 3C
Region I
Region II
Fig. 3B
N
C0 calculation (Fig. 3C)
A=1070 km²
10 km
A
Channel C0
MES
Channel C1
100 ms
1 km
C0 alluvial terrace
Wmax
Hmin
Hmax
Wmin
B
Quantitative analysis of hydrological dynamics
Discharge rates (Fig. 3A)
Region I
Region II
Q*C1=6969
Q*C2=3515
Q*C3=3595
QC1=14 789
≈ QTOT RI
QTOT RI =14 079m³/s
(m³/s ± 500)
Calculated Qmean (Table. S1)
Wmean (m) Hmean (m) Pmean (m)
C0 1200 21 2500
C1 296 12 323
Qmean (m³/s)
C0 240000
C1 7193
C
Depth [m]
-2000
-3000
-4000
erosion
Channel Knickpoints
mean slope <α> :
C1: 0.2°
C2: 0.43°
C3: 0.38°
exaggerated slope due to seismic migration
0 10 20 30 40 50 60
Distance upstream [km]
D
E
Discharge calculations for C1
Discharge (m³/s)
1787 historic flood
1907 historic flood
Qm (Manning formula)
Qu (Attal et al., 2008)
Q=3.7 A^0.41 | R²=0.77
Q=12.5 A^0.35 | R²=0.74
5000
10000
15000
2.10⁸ 4.10⁸ 6.10⁸
Drainage area (m²)
Stream length [m]
Flint's Law
ks: 8.1825
θ: -0.3063
Slope
10⁻²
10⁻³
Hack's Law
h exponent: 0.4840
8 6 4 2 0
F
10⁶ 10⁷ 10⁸ 10⁹
Area [m²]

Figure 4

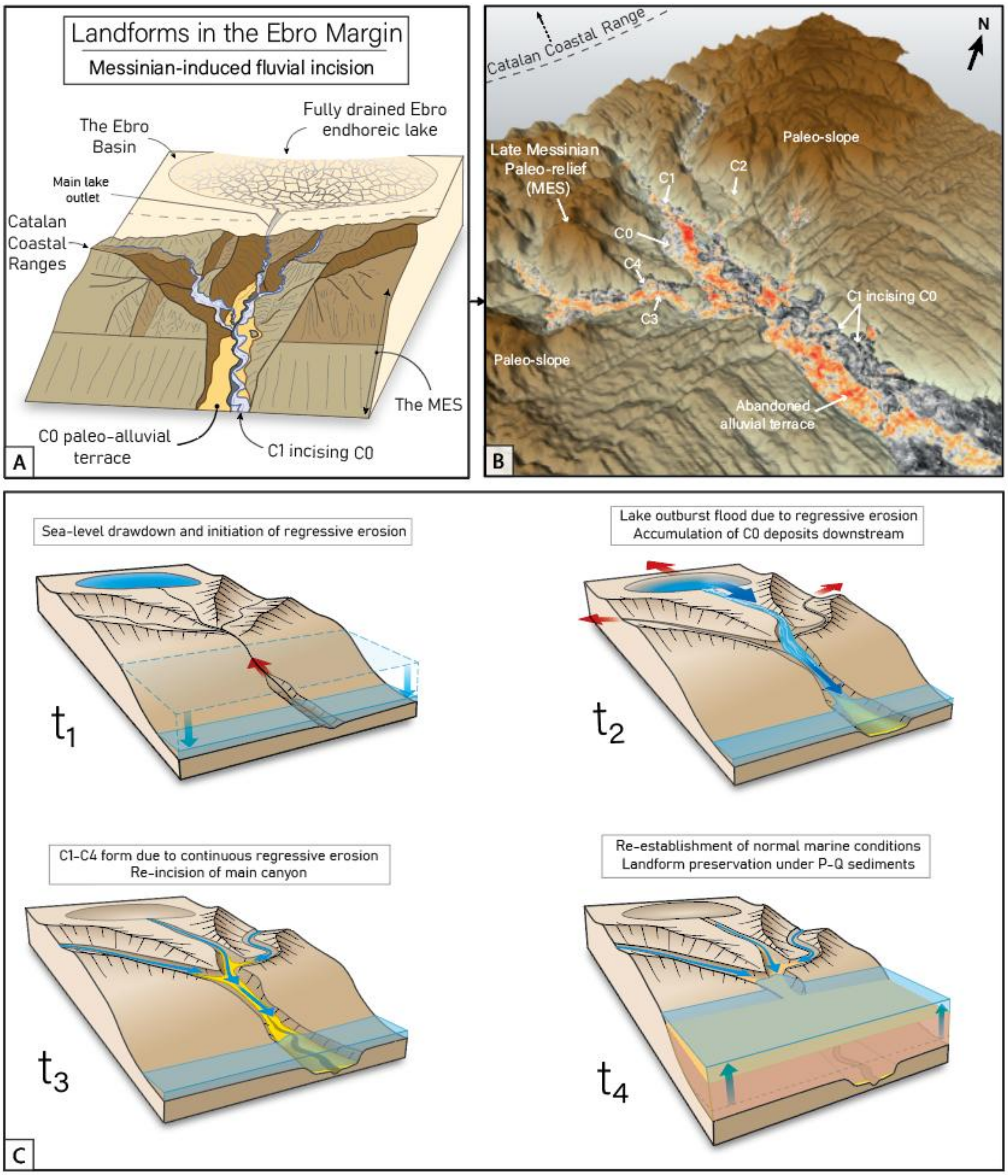

SUPPLEMENTAL MATERIAL

GSA DATA REPOSITORY

Supplemental Material for "Relict landscapes and fluvial landforms: Catastrophic outflow following a major Late Messinian base-level fall

Ninkabou D.[1,2], Gargani J.[3], Gorini C.[1], Rubino J-L.[2], Urgeles R.[4], Pellen R.[5], Do Couto, D. [1], Lethiers, A.[1], Haq, B.[1, 6], and Moneron, J. [1*] (corresponding author: jimmy.moneron@sorbonne-universite.fr)

[1] *ISTeP, Sorbonne Université, CNRS, 75005 Paris, France*

[2] *Total E&P, 92078 La Défense, France*

[3] *GEOPS, Univ. Paris-Saclay, CNRS, 91405 Orsay, France*

[4] *Institut de Ciències del Mar (CSIC), 08003 Barcelona, Spain*

[5] *LGO, Univ. de Bretagne Occidentale, CNRS, 29280 Plouzané, France*

[6] *Smithsonian Institution, Department of Paleobiology, Washington DC, USA*

ADDITIONAL DATA AND METHODS

Data and resolution

The studied 3D seismic survey spans over 2700km² offshore of the Ebro Delta. Data presented in this study are pre-stack migrated, with a bin size of 12.5 x 12.5 m and a 4 ms sampling interval, and are SEG normal polarity. The different horizons (MES and channel deposits) presented in this study were picked on SISMAGE, with manual and automatic propagation. The frequency of the seismic data around the studied horizon is centered on 50Hz, resulting in a resolution of up to 12.5 ±2.5 m for a 3000 m/s medium velocity.

Workflow

The Messinian erosional surface and associated fluvial deposits were mapped on a zero-phase 3D seismic data in two-way time. The Messinian erosional surface is modified from Urgeles et al., 2010. The fluvial deposits and its base were automatically propagated using SISMAGE-CIG™, a proprietary geophysical platform developed by Total SA. The obtained MES depth map was depth converted using the time-depth law provided by Urgeles et al., 2011: $D=1135T^{1.3643}$.

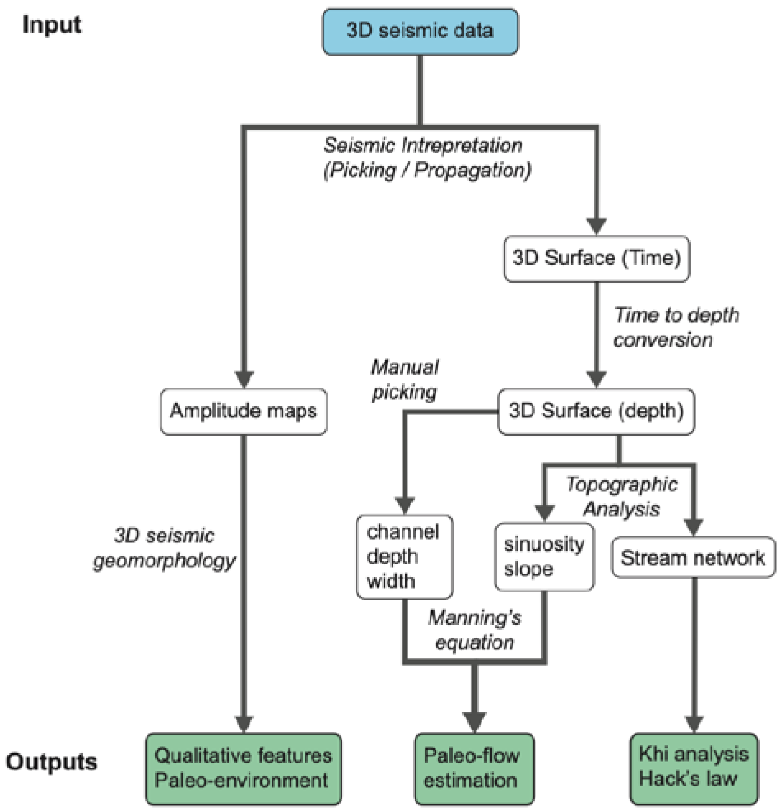

Figure 1: Workflow for the interpretation of the assessment of paleodischarge estimates on the Ebro margin

Topographic analysis and mean Discharge calculation

The depth converted map of the MES was analyzed with Topotoolbox (Schwanghart et al., 2014) to assess the features of the Messinian topography (Fig. 3). No post-depositional corrections were implemented to avoid the creation of errors and artifacts around fluvial morphology. Relative error on distances (height and width) is small and <50m of the measured distances (i.e. <5% for kilometric distances).

Quantitative analysis of hydrological dynamics was performed using Manning's equation (1) :

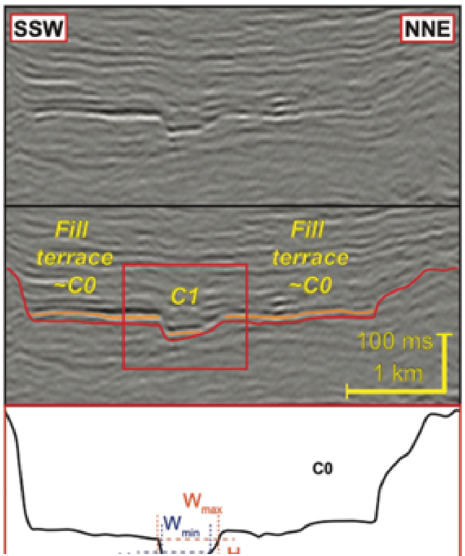

Figure 2 : From top to bottom: Uninterpreted seismic line. Interpreted seismic line showing the MES in red, and the associated fluvial system in orange. Bottom: Measurements used to assess the width and depth of the channel on depth sections, based on the presence of inflexion points on the channel geometry.

$$(1) \quad V = \frac{1}{n} R^{2/3} S^{1/2}$$

$$(2) \quad R = \frac{A}{P}$$

$$(3) \quad A = \frac{W \cdot H}{2}$$

$$(4) \quad Q = V \cdot A$$

where V is the flow velocity (m/s), R is the hydraulic radius, S the local slope and n the roughness coefficient equal to 0.05 (Garcia-Castellanos et al. 2009). The hydraulic radius R=A/P is calculated using the seismic data that allowed us to estimates the wetted perimeter P and the triangular section area of the channel A=W*H/2, with W the width as well as H the height of the channel. Then the water discharge Q=V*A was estimated on the main channels in various place from upstream to downstream.

We have estimated the mean megaflood discharge using the mean value of the discharge calculated in 2 different location. Concretely, we estimate on each location a minimum and a maximum discharges based on the geometry of the channel. Then the local mean value is used to calculate the average of the discharge.

We have also estimated the channel discharge of channel 2 using the measurements obtained in 5 different location along the meandering channel. Considering the 5 different measurements of the discharge, we assume geometries that allow us to not overestimate the discharge: the channel geometries inflexions have been considered as indicative of fluvial dynamic and used to estimate the height and the width of the channel instead of considering that the whole channel was full of water.

Discharge calculated from the width of the channels is based on the formula provided by Attal et al., 2008: $W= 4.6*Q^{0.5}$ (5). All results are in m^3/s.

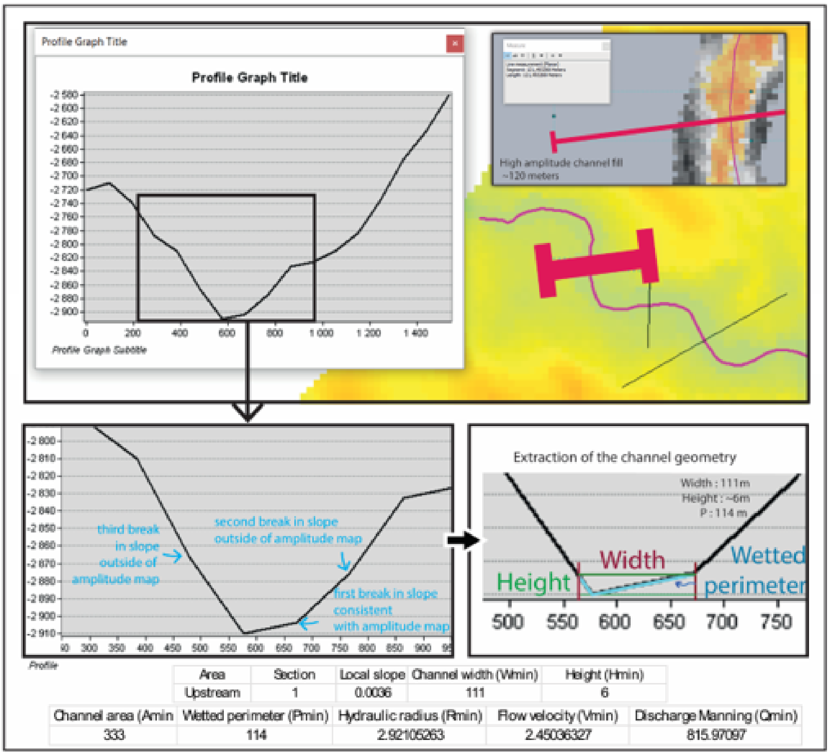

Figure 3: Workflow for discharge calculation

Erosion rate estimation

Erosion rate was estimated from the maximum relief observed in the basin (~1300m) and the onset of sea-level fall (5.60 Ma) to the Lowstand stage (5.46 Ma) for the Maximum erosion rate and flooding (5.36 Ma) for the Minimum erosion rate.

Results obtained: Max 140ka duration Min 240ka = [5.41 mm/yr; 9.28 mm/yr]± 2mm/yr.

Flexural isostasy calculation

Flexural isostasy *w(x,y)* is implemented considering the thin-elastic plate compensating for the unload generated by erosion and using the equation (Turcott and Schubert, 2001):

(6) $$\nabla^2\left(D\nabla^2 w(x,y)\right) + (\rho_a - \rho_s)g \cdot w(x,y) = \rho_s g\left[z_{ref}(x,y) - z(x,y)\right]$$

where is the missing material thickness after erosion, ρa and ρs are the densities of asthenosphere and sediment respectively, g the acceleration of gravity and D is the rigidity. The rigidity is described by the equation:

(7) $$D = \frac{ET_e^3}{12(1-\upsilon^2)}$$

ADDITIONAL RESULTS AND FIGURES

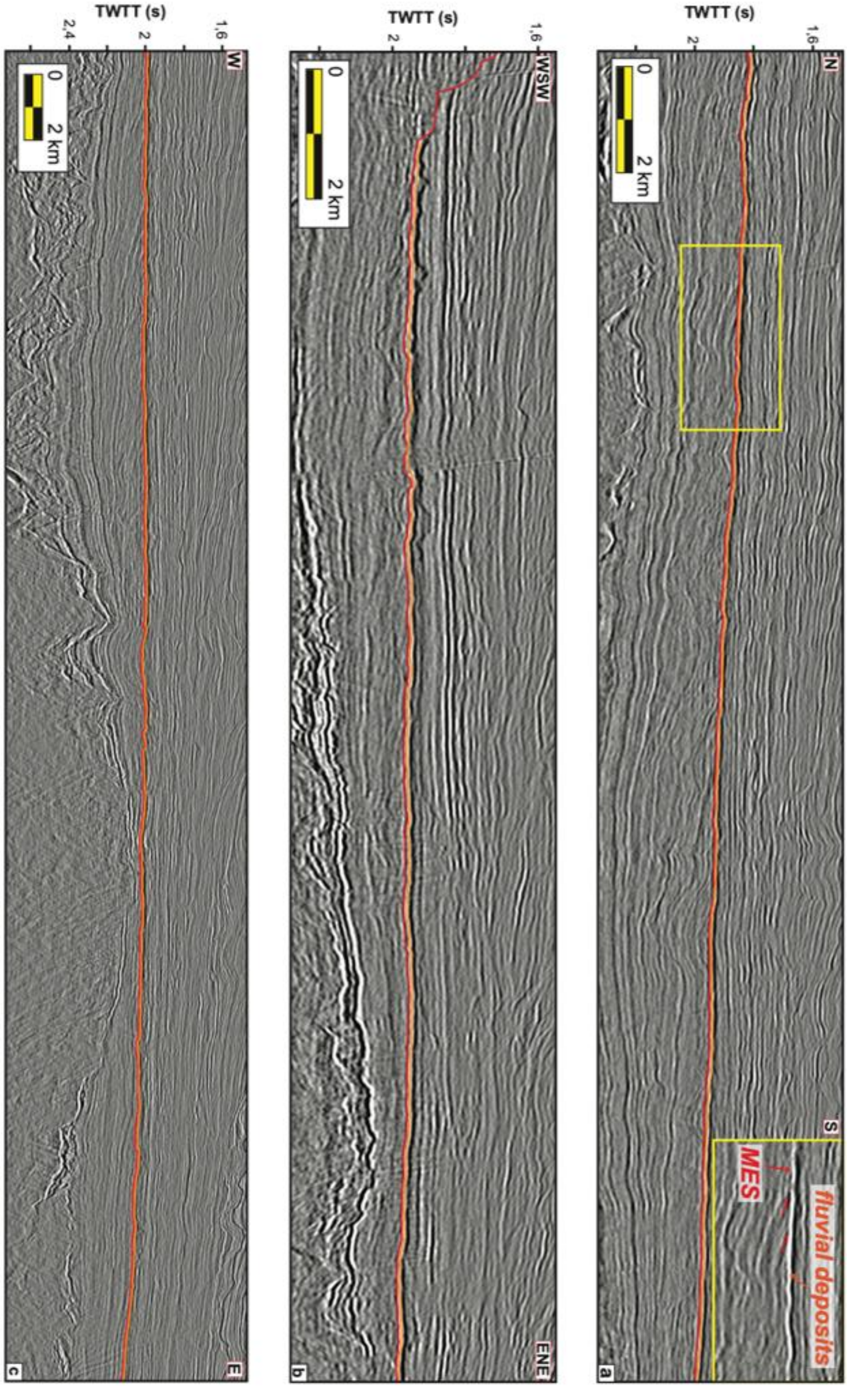

Figure 4: Seismic lines through the thalwegs of Channel C1 to C3

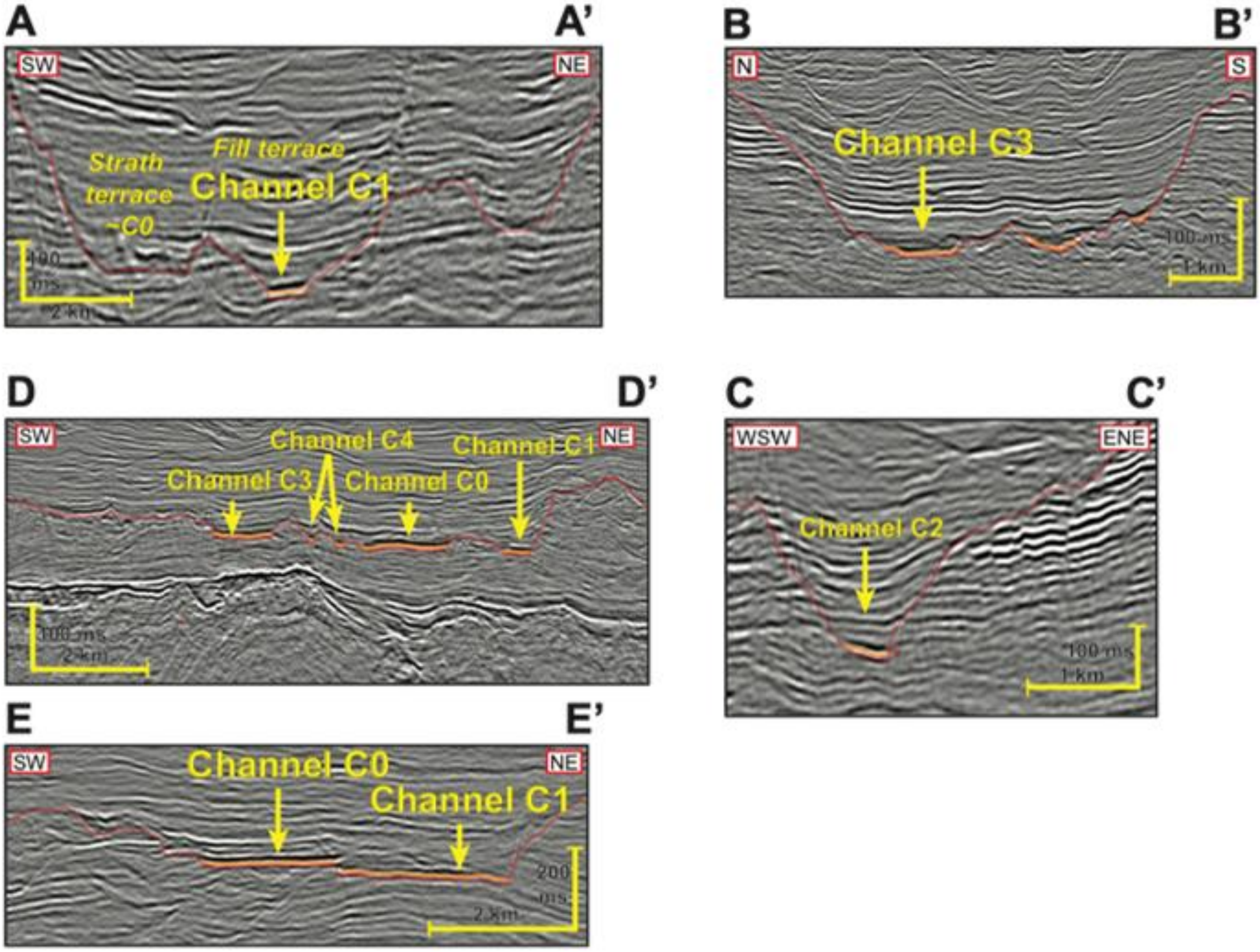

Figure 5: Seismic cross-sections of the Channel. profile locations on Fig. 1 of the article

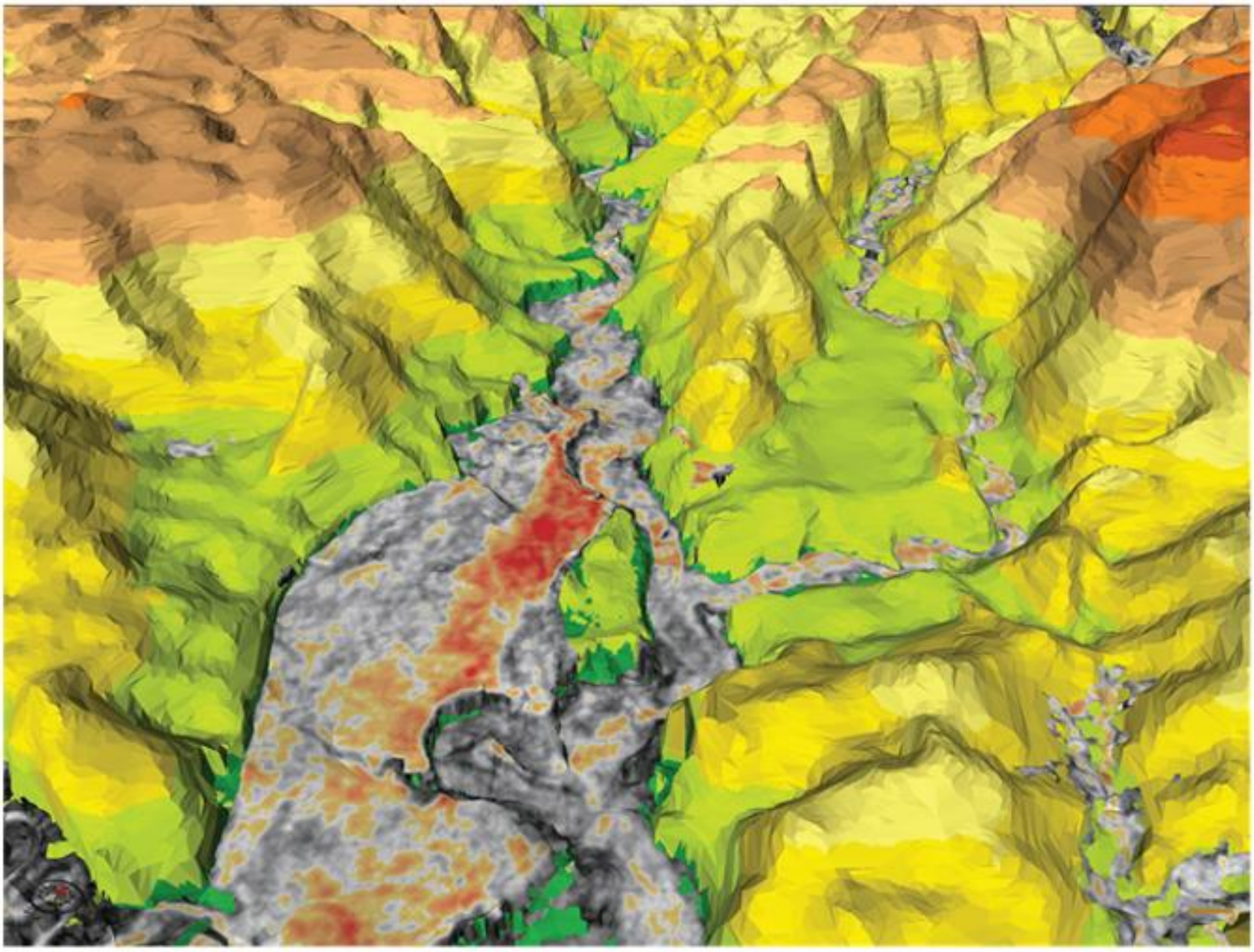

Figure 6: Unannotated 3D view of the picked fluvial system overlain on the MES. Here are shown the C0, C1 and C2 channels in the Region I of the MES

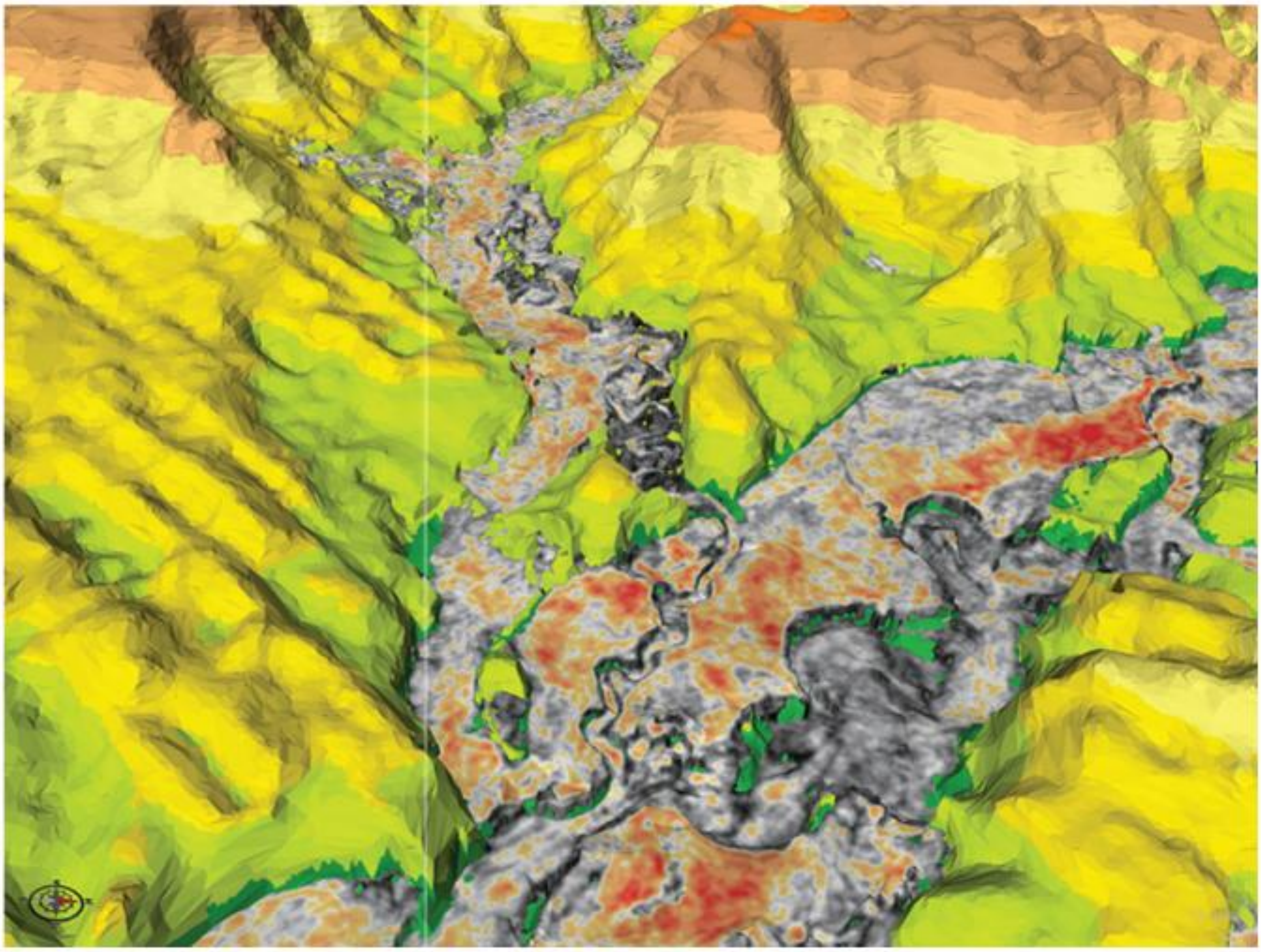

Figure 7: Another unannotated 3D view of the picked fluvial system overlain on the MES. Here are shown the C0, C1, C3 and C4 channels in the Region I of the MES

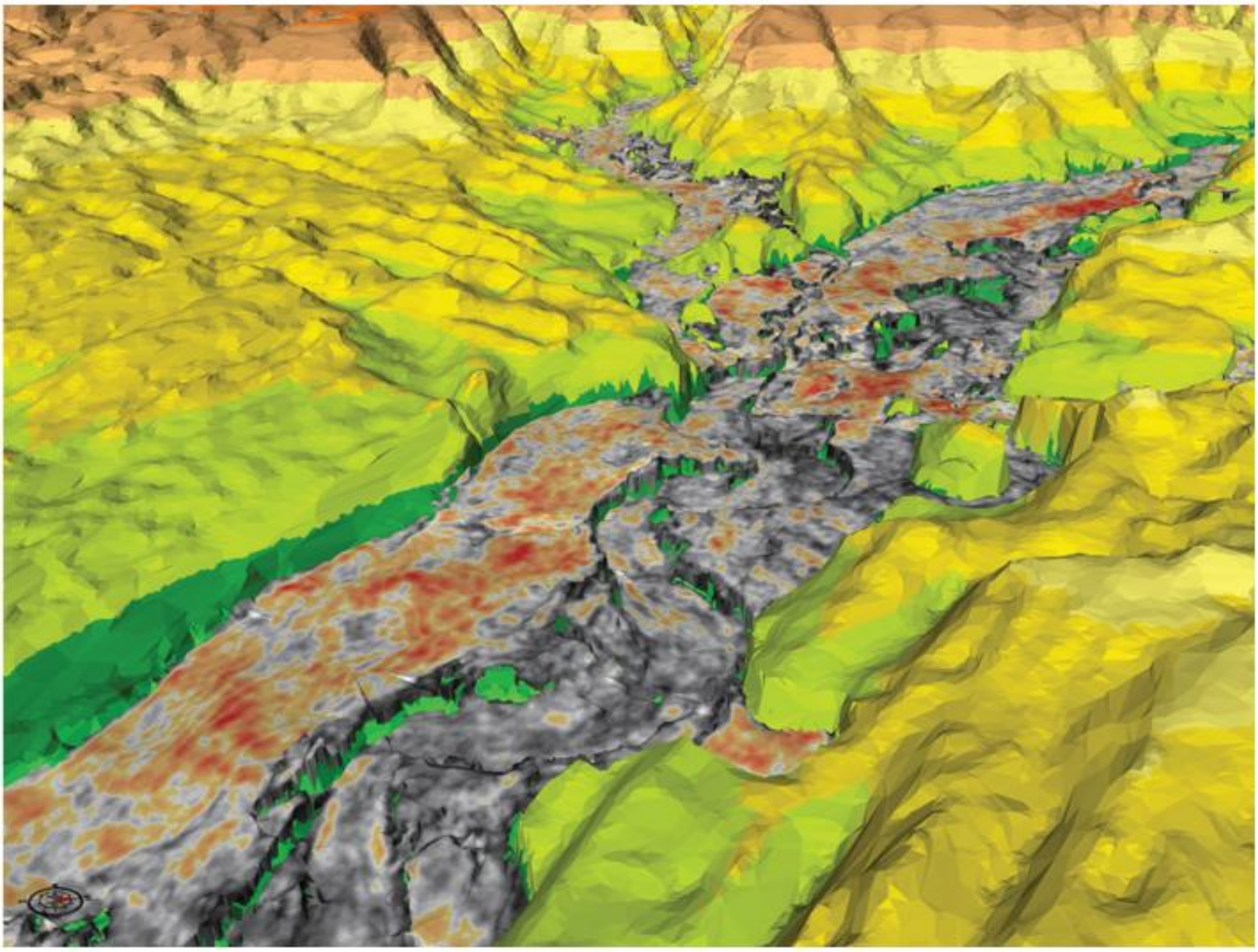

Figure 8: Unannotated 3D view of the picked fluvial system overlain on the MES. Here are shown the C0, C1, C3 and C4 channels in the Region I&II of the MES. Note how the C1 channel incised the C0 channel, and the difference in amplitude between both channels

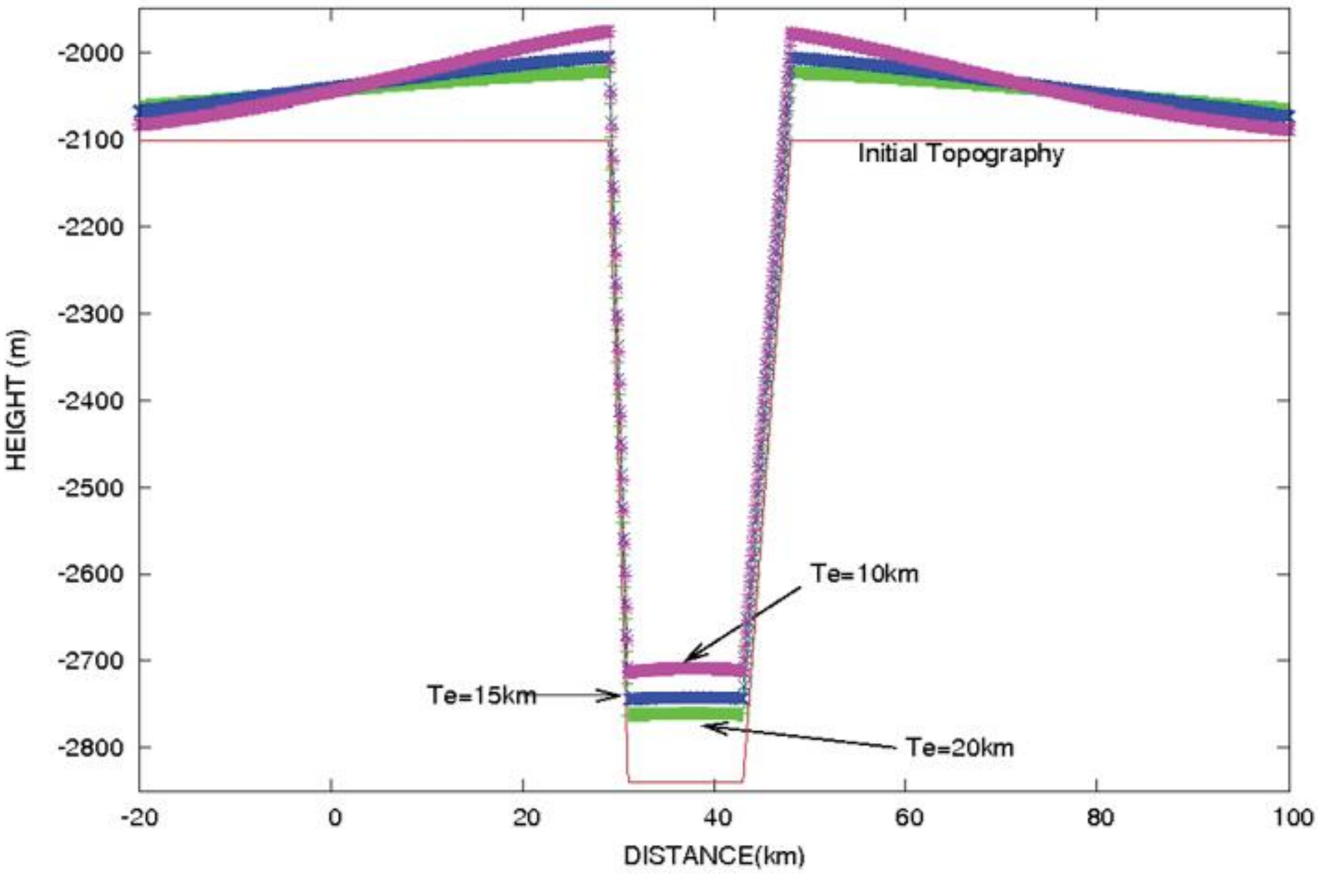

Figure 9: Calculation of the isostatic rebound linked to erosion based on profile BB' of Fig. 6. For an erosion of ~740m of bedrock, the isostatic rebound is estimated to be between 80 and 140m, with an initial elastic thickness ranging between Te=20km and Te=10km, respectively.

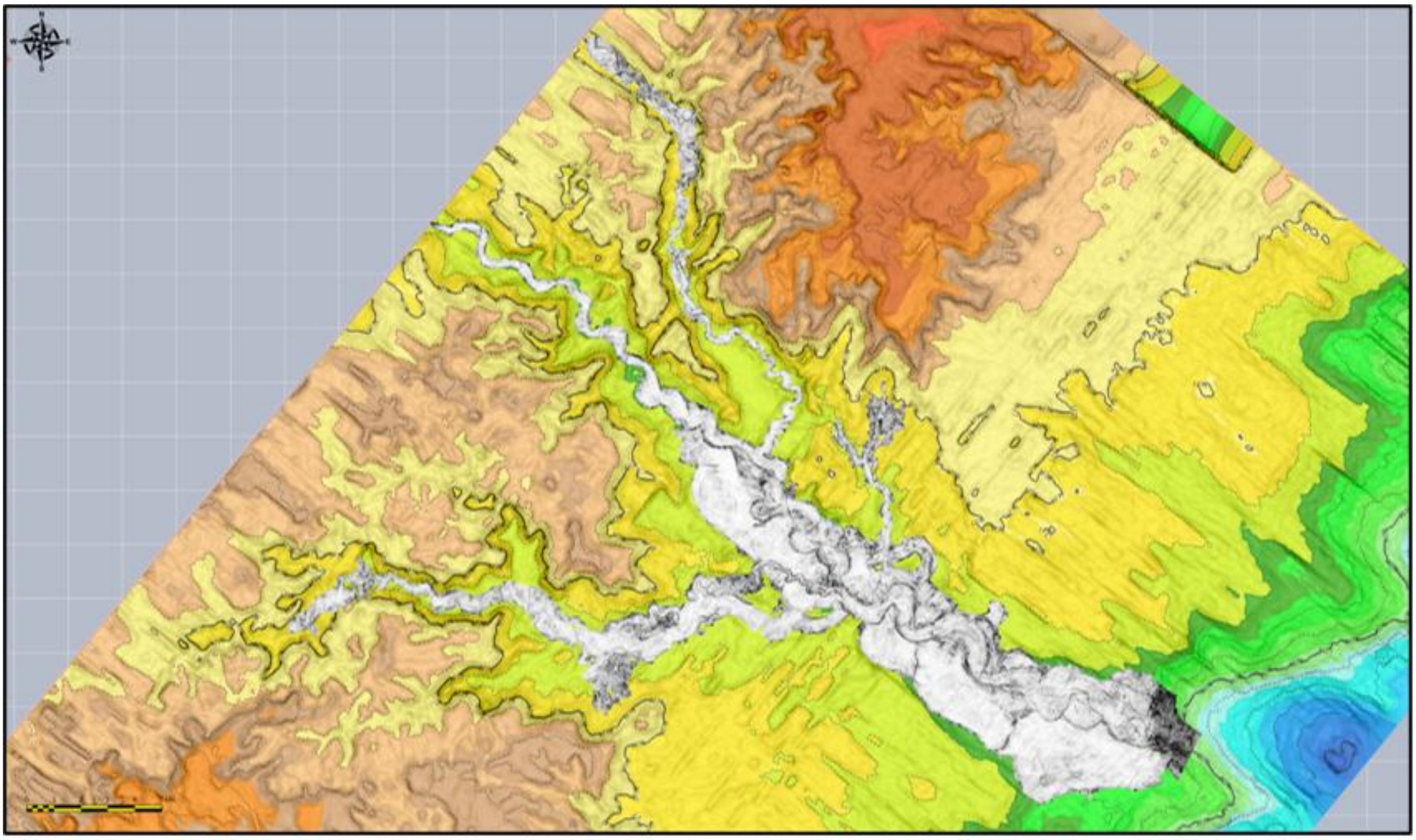

Figure 10: Uninterpreted version of Fig. 2A